iScience

CellPress
OPEN ACCESS

Article

Numerical investigation of a graphene-on-semiconductor device for optical monitoring of cell electrophysiology

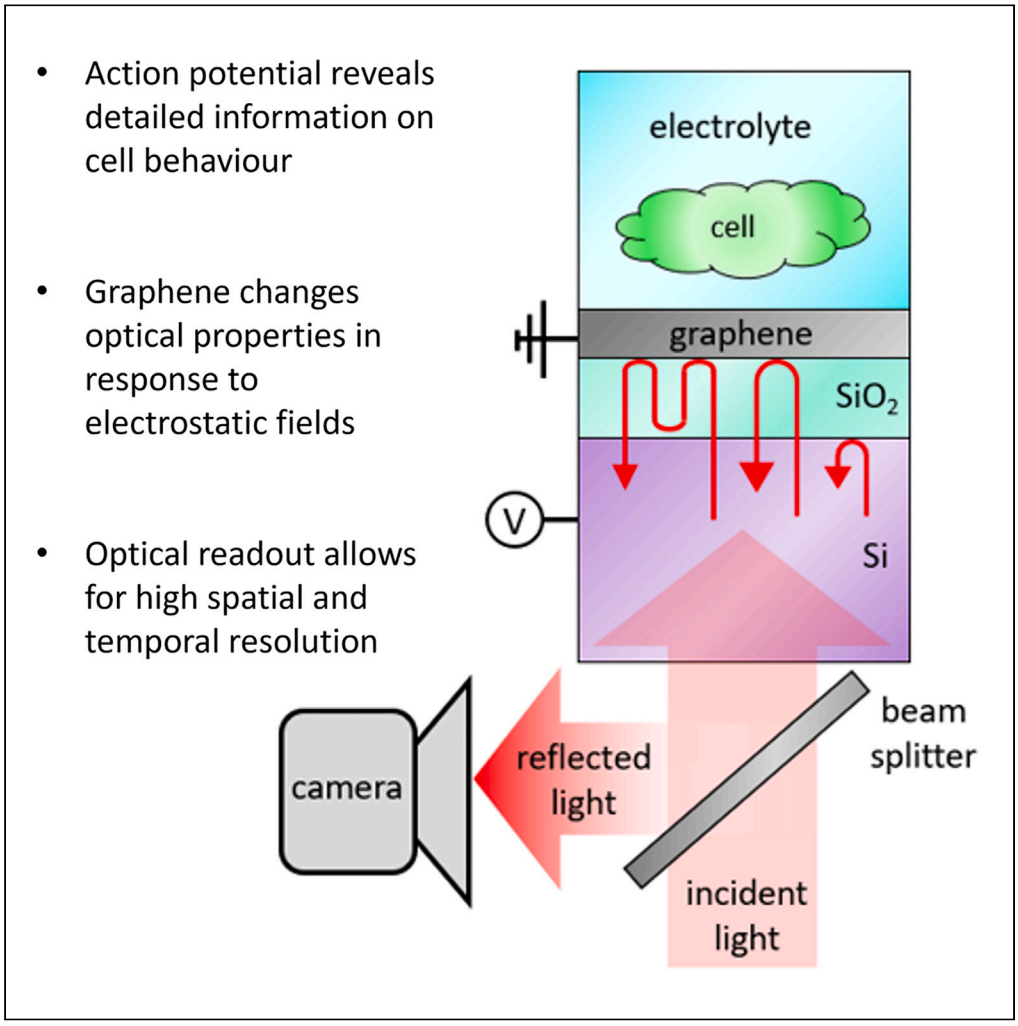

Jon Gorecki, Steffi Krause

j.gorecki@imperial.ac.uk

Highlights

Electrostatic fields around cells reveal information on cell processes

Current methods to measure electrostatic fields are slow or low resolution

Optical readout of electronic doping in graphene can provide fast, high resolution data

Gorecki & Krause, iScience *27*, 108554
January 19, 2024 © 2023 The Author(s).
https://doi.org/10.1016/j.isci.2023.108554

iScience

CellPress
OPEN ACCESS

Article

Numerical investigation of a graphene-on-semiconductor device for optical monitoring of cell electrophysiology

Jon Gorecki[1,3,*] and Steffi Krause[2]

SUMMARY

Spatially resolved sensing devices for electrostatic potentials are extremely useful for characterization of living cells, however, many current techniques lack the speed necessary to capture spatially resolved, functional information of cells in real-time. Here, an optical sensing technique is proposed based on graphene on a semiconductor stack operating in the near-infrared spectrum. By modeling coherent interference of multiply reflected beam paths within the semiconductor stack, we demonstrate how the device produces a continuous reflectivity change in response to graphene Fermi energy which is ideal for sensing changes in local electrostatic fields produced by action potentials of living cells. By coupling the device with a high-speed camera, we propose this platform will allow for high-speed imaging of action potentials over a large sensing area with micron scale resolution.

INTRODUCTION

Measurement of the electrostatic environments surrounding cells provides a wealth of information on physiological processes such as neuron signaling,[1–3] ion channel states,[4,5] and interactions of pharmaceuticals with cells.[6] There are a wide range of available methods to measure these electrophysiological signals, each with their own distinct advantages and drawbacks. The patch clamp amplifier is a method to measure electrical currents in cells and is considered the 'gold standard', providing high sensitivity measurements of individual cells.[7] The main drawbacks to this technique are that it is work-intensive and requires a probe to be placed into a cell, and therefore does not allow measurement of multiple cells simultaneously with spatial resolution. Microelectrode arrays (MEAs) allow for many individual electrical sensors to be patterned onto a substrate, and can achieve sensor densities around 1 sensor per 10 μm.[8] The sensors demonstrate good sensitivity[9] and benefit from a large crossover with the mature fabrication technology of thin-film transistor (TFT) televisions; however, as each sensor requires individual electrical contacts it leads to complicated fabrication and many measurement channels are required to record the signals. To overcome the issues to multiple electrodes with independent electrical readout, it is possible to use light addressable electrode technologies such as light addressable potentiometric sensors (LAPS).[5,10–12] The LAPS technique utilizes an insulated planar semiconductor substrate in which a focused modulated laser locally creates photocarriers within the space charge layer of the substrate. By electrically biasing the substrate an alternating current is measured, which depends on the potential near the surface of the insulator. By scanning the laser over the surface, a 2D map can be built up of the surface charge.

Optical techniques (see here for recent review[13]) have also been used as they remove the need to individually address each 'sensor' and instead perform a wide area spatially resolved detection with an optical sensor (such as a camera) which can be purchased commercially. Fluorescent dyes (fluorophores) are optically activated by short wavelength light (often in the blue-green region) which undergoes a molecular energy shift and re-emits light at a longer wavelength.[14–16] They are extremely useful as one can use tailor the fluorophores to bind to specific biomolecules, and using fluorophores with different emission wavelengths allows for easy identification and characterization. Voltage sensitive dyes[17–19] are able to alter their spectral properties in response to local voltage changes. Both fluorescent and voltage sensitive dyes are extremely useful as they have a high degree of penetration through tissue and versatile applications, however, they can cause long term physiological changes to cells and even cytotoxicity. Pristine graphene sheets are an excellent material for investigating the electrophysiology of cells as they demonstrate a high degree of biocompatibility,[20] and allows for good cell adhesion.[21] Recently a device consisting of graphene on multilayered semiconductor substrate has been demonstrated for optical measurement of bioelectric potentials.[22] The device utilizes the semiconductor layers as a thin waveguide for oblique incident light. The graphene top-layer (at the semiconductor - electrolyte interface) experiences a local change in electrical properties in response to electrostatic fields of the cells, which alters the coupling conditions of the waveguide device, and causing large changes in the reflectivity which can be measured in a spatially resolved manner with a CCD array. Measurements were performed on cells, revealing 1% reflectivity changes in response to action potential, which can be seen to move spatially

[1]Department of Bioengineering, Imperial College London, Exhibition Road, London SW7 2BX, UK
[2]School of Engineering and Materials Science, Queen Mary University of London, Mile End Road, London E1 4NS, UK
[3]Lead contact
*Correspondence: j.gorecki@imperial.ac.uk
https://doi.org/10.1016/j.isci.2023.108554

This is an open access article under the CC BY-NC-ND license (http://creativecommons.org/licenses/by-nc-nd/4.0/).

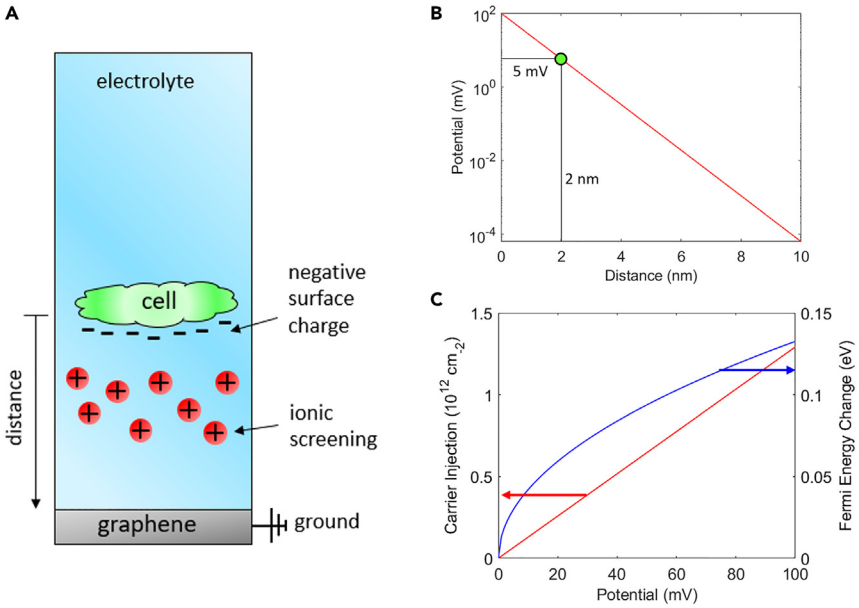

Figure 1. Electrostatic screening effect on charged cell, and corresponding changes to electronic properties of graphene

(A) Schematic diagram depicting a cell with charged surface in an electrolyte solution, in close proximity to graphene monolayer. The electrostatic charge of the cell will result in an ionic screening effect in the electrolyte.

(B) Decaying potential due to ionic screening effect as a function of distance away from the cell.

(C) Change in graphene Fermi energy and carrier density in response to cell potential.

through a cell cluster. Due to the oblique illumination angle and the multiple reflections within the waveguide structure the resultant images contained a smearing effect where multiple reflected images were appeared to overlay and slightly offset along the direction of illumination. This artifact limits the ability to spatially resolve fine details in the images, yet was a necessary condition to achieve guiding within the waveguide structure.

Here a graphene device is modeled for its applications in sensing action potential of cells in ionic solution, which consists of a thick silicon substrate covered with thin silicon dioxide and a graphene monolayer. By analyzing the graphene light interactions in terms of inter and intraband transitions and modeling multiple internal reflections within the thin silicon dioxide layer it is shown that by tailoring the silicon dioxide layer thickness it is possible design a device which, when illuminated from the back silicon side, will alter the strength of its reflection to an incident beam of 1560 nm by $\sim$ 1%, which is of similar magnitude to other demonstrated optical methods. Further, it is shown that illumination with a shorter wavelength of 800 nm will render the device reflection insensitive to action potential, which enables a method for referencing and normalizing the data. We propose that this platform will allow for superfast recording of electrostatic potentials over a large area with high resolution, which will be capable of capturing detailed information on cell interactions such as signaling in neuron networks.

Electrostatic field magnitudes

To investigate the potential applications for electrostatic sensing devices based on graphene it is essential to first understand the nature of the electrostatic environment which will be encountered. In Figure 1A a schematic diagram is presented which depicts a cell in electrolyte solution located at a discrete separation distance away from an electrically grounded graphene sheet. The cell has a net negative electrostatic charge. When an electrostatically charged object is surrounded by an ionic solution a screening effect will occur in which the oppositely charged ions of the solution are electrostatically attracted to the object. The screening effect can be simply modeled by using the Debye length, which characterizes the length at which a potential voltage will be reduced by a factor of $1/e$ by the screening effect. In physiological buffer solutions, the Debye length is $\sim 0.7nm$.[23,24]

First, we must establish how close a cell could come to the surface of the graphene. Via use of transmission electron microscopy, cells cultured on flat surfaces have been measured to have separations in the region of 40–100 nm, measured as the distance from cell membrane to surface.[25] When cells are cultured to surfaces they attach by protruding focal adhesions, which leave a layer between the cell and the surface that then fills with liquid and causes ionic screening. At this distance the ionic screening effect is massive and electrostatic fields at the semiconductor surface would be negligible, and therefore further engineering is required to overcome this issue.

In the work of Jacques[26] photoelectrochemical measurements are performed on cardiomyocytes; in one experiment cells are cultured directly onto the semiconductor surface, while in the second experiment cardiomyocyte organoids (cultured in suspension) are mechanically pressed against the surface. It is found that the surface-cultured cells exhibit near undetectable photo-electrochemical signal (due to ionic screening), while the mechanically pressed cells can be individually located by their electrostatic fields, allowing their action potentials to

be recorded. It is believed this effect is possible as the mechanically pressed cells have not formed focal adhesions and can therefore approach closer to the semiconductor surface. In this work average action potential amplitudes of 8 mV were measured, while similar cells have been measured with patch clamp amplifier techniques in a range of electrode geometries and found action potentials ~ 100 mV on the cell surface.[9] By taking the Debye length as 0.7 nm, and a conservative nominal value of the screened action potential as 5 mV, it is found that an action potential of 100 mV would be reduced to this nominal value over a distance of 2 nm as shown in Figure 1B. The value of 2 nm separation is used here to investigate the possibility of using graphene as a sensing surface for action potentials. It is interesting to note that this distance of 2 nm is very similar to that of the distance between two cell membranes observed in cell junctions,[27] therefore it is not unrealistic that a cell could come to such proximity to a semiconductor surface. Vibration isolation may be required to avoid mechanical noise and keep the applied pressure constant when applying mechanical pressure to cells.

The charge carrier injection into graphene can be described by Equation 1, where n_0 is the number of injected carriers per m^2, ϵ_r is the relative permittivity of the separating medium, ϵ_0 is the vacuum permittivity, V is the potential difference given in volts, d is the distance given in meters, and e is the elementary electron charge given in Coulombs. In practice n is more often quoted in units of cm^{-2}, where a carrier injection on the order of 10^{12} cm^{-2} constitutes a significant carrier injection into a graphene monolayer.

$$n_0 = \frac{\epsilon_r \epsilon_0 V}{ed} \quad \text{(Equation 1)}$$

For the case of electrostatic gating of graphene in an ionic solution Equation 1 is modified to include an exponential damping term characterized by the Debye length, shown in Equation 2, where λ is the Debye length (given here a nominal value of 0.7 nm).

$$n = \frac{\epsilon_r \epsilon_0 V}{ed} exp(-d/\lambda) \quad \text{(Equation 2)}$$

The Fermi energy of the graphene E_f is given by Equation 3, where $\hbar$ is the reduced Planck constant, and V_f is the Fermi velocity of graphene (10^6 m/s). This value of Fermi velocity has been experimentally determined for polycrystalline graphene and exfoliated sheets, and has been found to be similar in both cases.[28]

The resultant Fermi energy is given in SI units, however, it is conventional to convert this to electron volts by dividing by the elementary electron charge. Typical values for graphene Fermi energy are in the region of ±1 eV, where a change on 0.1 eV would produce significant and measureable alteration in the optoelectronic properties of graphene. Figure 1C plots the change in Fermi energy against potential (at the surface of the cell), for the nominal case of a 2 nm separation between graphene and charged object. From this graph we see that the action potential of a cell (brought into close contact to the surface by mechanical force) is capable of inducing significant changes to the graphene Fermi energy of 0.13 eV in response to a 100 mV action potential.

$$E_f = \hbar V_f \sqrt{\pi n} \quad \text{(Equation 3)}$$

Interactions of graphene with light

The interactions of light with a graphene monolayer in the presence of an electrostatic field can be easily defined by the Kubo equations to describe the AC conductivity[29] as a function of wavelength and Fermi energy, whereby the Fermi energy can be tuned by a local electrostatic field. An in-depth description is provided in Section S1. Once the AC conductivity is calculated the reflection coefficient can be calculated by the Tinkham equations as shown in Section S2.

Considering the case of a graphene monolayer on a thick silicon substrate with initial graphene Fermi energy of 0.3 eV and a nominal Fermi energy change of 0.1 eV, we investigate the resultant change in reflected intensity as a function of incident wavelength (Figure 2A). At visible wavelengths (< 1 μm) it can be seen that the reflectivity change is extremely small (< 10^{-4} %) which would make sensing applications difficult. This is unfortunate because at visible wavelengths sensing equipment and light sources are extremely well developed commercially, and the short wavelength allows for high resolution imaging. At the other end of the scale around 100 μm (which corresponds to the crossover of the long infra-red into the THz region) it can be seen that the sensitivity is far higher, however, at this wavelength the resolution of a sensing device would be far too large for useful application to cells. In the intermediate region (1–3 μm) it can be seen there is a broad, flat topped, feature which peaks with a maximum reflectivity change around 1 %. This feature is due to the cross-over point between inter-band and intra-band transitions in the graphene.

In Figure 2B this feature is investigated further by plotting the change in reflectivity at 1560 nm as a function of graphene Fermi energy (which can be altered by a local electrostatic field). It can be seen that at low Fermi energy the reflectivity is a flat constant value, which abruptly increases by nearly 1% in a sharp step-like feature. This response is not desirable for sensing applications as it would return only a binary response between high and low Fermi energy, whereas the ideal response would be a continuous linear change. To overcome this issue, we investigate how this device response can be improved by incorporating multiple semiconductor layers to utilise coherent interference effects.

Device optimization

Figure 3A shows a schematic diagram of a proposed device consisting of a thick slab of silicon ($\tilde{n}$ = 3.5 + 0i), followed by a thin layer of silicon dioxide ($\tilde{n}$ = 1.47 + 0i) with thickness d (155 nm), covered with a graphene monolayer. Silicon and silica are chosen here as they both exhibit

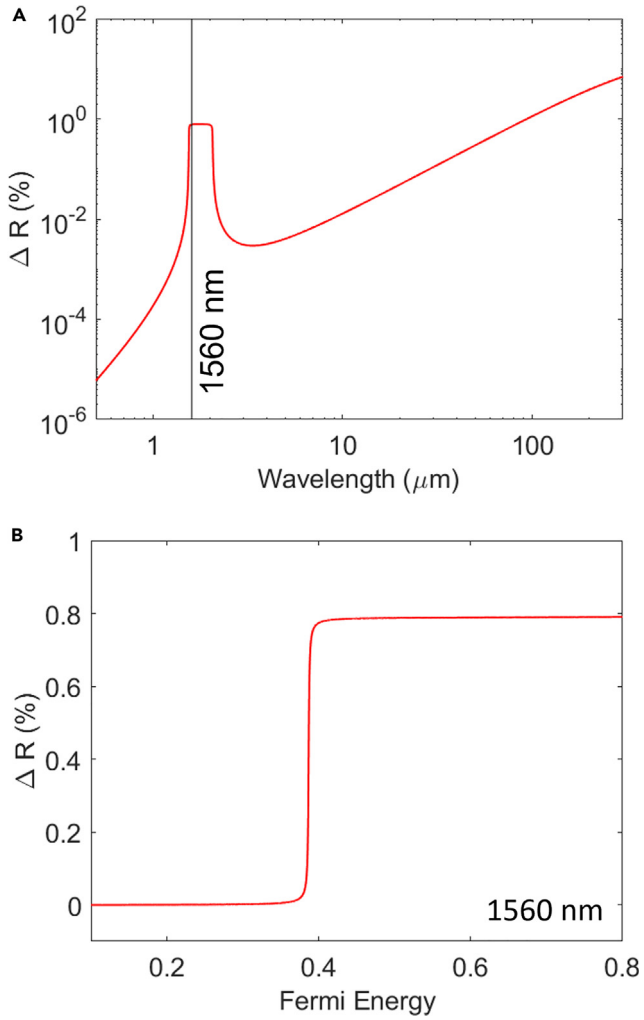

Figure 2. Reflectivity changes for intrinsic graphene monolayer

(A) Reflectivity change vs. wavelength for silicon substrate covered with graphene layer increasing Fermi energy from 0.3 to 0.4 eV.

(B) Reflectivity change vs. Fermi energy for an incident wavelength of 1560 nm.

high transparency and low values of absorption in the NIR region.[30] When illuminated with a 1560 nm coherent source from the silicon side light will undergo multiple reflections within the silicon dioxide layer. The first three reflection paths are depicted with red arrows, however, in reality this will extend to infinity. There are no reflections within the graphene monolayer as it is too thin to support internal reflections. On the other hand, the silicon layer is too thick to allow for internal reflections to be coherent (for optically thick substrates the surface parallelism and roughness prevent internal reflections from interfering coherently).

The first pulse is reflected by the silicon - silicon dioxide interface, which is described by the Fresnel reflection equation. The second pulse is transmitted through the silicon - silicon dioxide interface (described by Fresnel transmission equation), is exponentially attenuated while passing through the silicon dioxide slab, reflects off the graphene (described by the Tinkham equation), then passes again through the silicon dioxide slab, and the silicon dioxide - silicon interface. Subsequent pulses (as shown for the third pulse) will reflect multiple times within the silicon dioxide and will therefore contain increasingly more interaction terms. Section S2 of the supplementary section describes in detail how the reflection values are calculated.

Figure 3B plots reflectivity (subtracted from the maximum reflectivity) for the device for two different thicknesses of silicon dioxide layer. It can be seen that by including the additional silicon dioxide layer the reflectivity profile has changed from a sharp step feature into a smoother response over a wide range of Fermi energy values. There is also a large dependence in the response shape and magnitude upon the thickness of the silicon dioxide layer. This thickness effect is investigated in Figure 3C where the reflection percentage (subtracted from the maximum reflection for each thickness value) is plotted as a color plot against thickness of silicon dioxide layer and Fermi energy for an incident wavelength of 1560 nm. It can be seen that close to 0.4 eV there is a sharp transition which corresponds to the maximum rotation angle. An optimum thickness of 155 nm is chosen as this provides the largest change in reflection on either side of the Pauli blocking feature. Figure 3D explores how the device

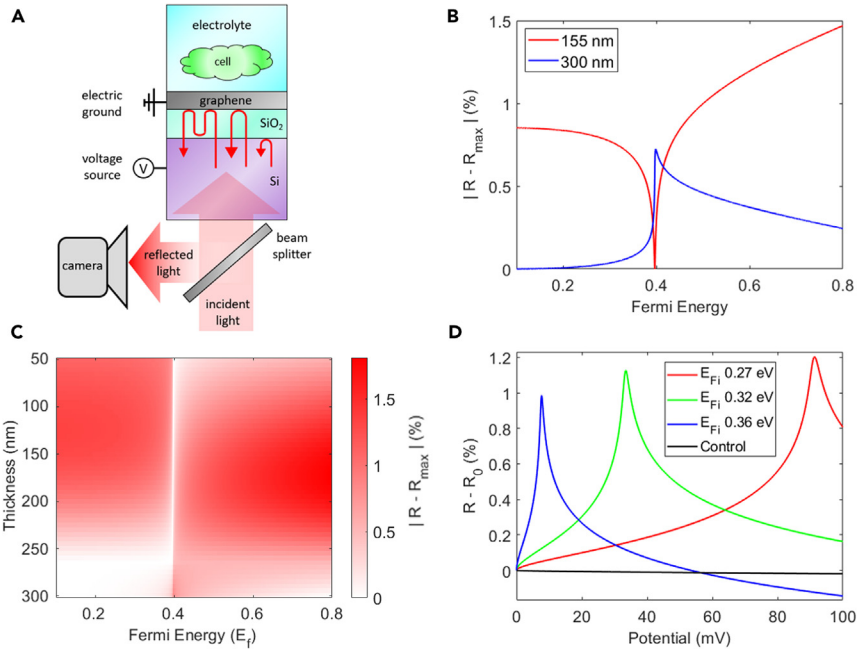

Figure 3. Design of a sensing device based on layered semiconductor/graphene stack to broaden the sensitivity region

(A) Schematic diagram of a Si-SiO_2-graphene-electrolyte with top-down illumination. Multiple coherent reflections are created within the SiO_2 layer.

(B) Reflection intensity plotted against Fermi energy for case of Si-graphene and Si-SiO_2-graphene, for two different SiO_2 thicknesses. The addition of the SiO_2 layer results in a smooth change in reflection over a broader range of Fermi energies.

(C) Reflection plotted against SiO_2 thickness and Fermi energy reveals reflection intensity magnitude strongly depends on thickness of SiO_2 layer, where the optimum reflection is seen at a thickness of 155 nm.

(D) Reflection intensity plotted against potential for a range of initial Fermi energies.

would respond to an action potential of a cell at 2 nm separation with ionic screening effects. The red, blue, and green curves plot the reflection changes for a range of initial graphene Fermi energies at 1560 nm. It can be seen that depending on the initial Fermi energy the graphene can be tuned to become sensitive to different values of potential. By electrically connecting the silicon layer to a voltage supply the initial Fermi energy of the graphene can be tuned to the desired starting condition. In black the reflection changes are plotted for an initial Fermi energy of 0.34 eV when illuminated at 800 nm. It can be seen that when illuminating with a wavelength/Fermi energy combination far from the Pauli blocking feature there is negligible change in reflection in response to potential. This effect is useful as it can allow for a reference measurement for example if two detectors are used with narrow band filters. The optimized device produces ~ 1 % change in reflectivity in response to a 100 mV potential (a typical value for the action potential of a cardio myocyte) which is of similar magnitude to other optical sensing techniques.[11]

DISCUSSIONS

Future work will involve the experimental fabrication and characterization of this device. The proposed fabrication route is to obtain commercial CVD (chemical vapor deposition) graphene on SiO_2 on silicon, or to thermally grow a silica layer vie thermal evaporation to the desired thickness, and coat with CVD graphene on polymer substrate. This fabrication route is simple and will be able to produce sensing devices with large sizes as commercial CVD graphene can be produced with areas larger than several square centimeters. A further advantage of the proposed optical sensing scheme is that the electrical sensing does not need any further fabrication (such as electrode arrays) as it can be accomplished by a commercially available camera which will allow for high pixel count and fast data recording on millisecond timescales. Modern commercial NIR cameras can achieve maximum frame rates of hundreds of Hz. From electrostatics simulations presented in Section S3 we find that the electrostatic doping effect could differentiate between multiple charged objects in close proximity with minimal cross-talk, which could therefore be used to image action potentials from multiple cells simultaneously. We find that the spatial resolution of such a device is 4 μm.

It is important to note that the reflection changes presented here are highly dependent on the separation between a cell and the graphene surface due to the ionic screening effect where any electrostatic field will decay exponentially over the Debye length. Although this may appear to be a limiting factor in the device the distance dependence could be overcome in the time domain as the electro-migratory behaviors of ionic solutions are highly dependent on the electric field modulation frequency due to the finite size and therefore finite diffusion speeds of ions in solution. Above MHz frequencies (μs timescales) the ionic solutions move from a Debye screening regime to being more suitably modeled as a dielectric insulator[31,32] which would dramatically increase the electrostatic gating effects in the absence of screening. Indeed, graphene transistor devices have been demonstrated for operation at high frequencies to overcome this specific issue.[33] Practically these measurements could be achieved by replacing a typical camera with a Single Photodiode Avalanche Detector (SPAD) which

can produce spatially resolved images with nanosecond time resolved information. This leads to the possibility of investigating a wide range of fast electrophysiological processes[34] in a spatially and time resolved manner without the limitation of ionic screening.

In future experimental verification of such a device it will be essential to characterize the achievable signal-to-noise ratio (SNR) as this will allow us to determine the minimum Fermi level changes that will be measurable. Future development of the graphene sensing effect could investigate the use of patterned graphene which could sustain plasmonic resonances in the IR region. By using plasmonic resonances it is possible to greatly enhance the sensitivity of the spectral response to the Fermi energy change, however to produce such geometries would require more in-depth fabrication procedures.

Conclusions

In this work graphene on semiconductor devices were proposed as a spatially resolved sensing platforms for action potentials. The response of the graphene devices is investigated by calculating the reflected intensity as a function of graphene Fermi energy, which can be tuned by local electrostatic fields (action potentials). It is shown that to produce a sensing device with a smooth response over a wide range of Fermi energies it is essential to use graphene on layered semiconductor stacks, as the inherent properties of graphene alone are unsuitable for this task. In this manner the multiple reflections within the layered semiconductor stack coherently interfere with each other and result in a smooth response over a wide range of Fermi energies. We investigated a stack consisting of silicon - silica - graphene, and demonstrated that the optimal device performance can be obtained by a silica thickness of 155 nm. Future work will involve experimental verification of this effect could produce spatially resolved measurements of action potentials with milli-second resolution, which will be of interest to researchers investigating electro-physiologically active cells.

Summary of supplementary information

Supplementary information is available for this publication which includes; S1: theoretical discussions on graphene conductivity, S2: a derivation of the graphene-semiconductor-stack reflection, S3: finite element simulations investigating the spatial resolution of graphene electrostatic gating, S4: MATLAB scripts for producing figures presented in the paper.

Limitations of the study

The work presented in this study utilized published reports of real-world values for physically measured parameters to theoretically model a proposed sensing device. The sensing device described in this paper has not yet been experimentally verified.

STAR★METHODS

Detailed methods are provided in the online version of this paper and include the following:

- KEY RESOURCES TABLE
- RESOURCE AVAILABILITY
  - Lead contact
  - Materials availability
  - Data and code availability
- EXPERIMENTAL MODEL AND STUDY PARTICIPANT DETAILS
- METHOD DETAILS
  - Calculation of graphene conductivity
  - Calculating device reflectivity
  - Determining device spatial resolution
- QUANTIFICATION AND STATISTICAL ANALYSIS

SUPPLEMENTAL INFORMATION

Supplemental information can be found online at https://doi.org/10.1016/j.isci.2023.108554.

ACKNOWLEDGMENTS

We thank the past and present members of the S. Krause research group for informative discussions. There is no specific funding associated with this work.

AUTHOR CONTRIBUTIONS

Conceptualization and Writing by J.G. Supervision and Advice by S.K.

DECLARATION OF INTERESTS

The authors declare no competing interests.

Received: April 17, 2023
Revised: September 19, 2023
Accepted: November 20, 2023
Published: November 24, 2023

REFERENCES

1. Morin, F.O., Takamura, Y., and Tamiya, E. (2005). Investigating neuronal activity with planar microelectrode arrays: achievements and new perspectives. J. Biosci. Bioeng. *100*, 131–143.
2. Obien, M.E.J., Deligkaris, K., Bullmann, T., Bakkum, D.J., and Frey, U. (2014). Revealing neuronal function through microelectrode array recordings. Front. Neurosci. *8*, 423.
3. Nam, Y., and Wheeler, B.C. (2011). In vitro microelectrode array technology and neural recordings. Crit. Rev. Biomed. Eng. *39*, 45–61.
4. Berridge, M.J., Bootman, M.D., and Lipp, P. (1998). Calcium - a life and death signal. Nature *395*, 645–648.
5. Zhou, B., Jiang, Y., Guo, Q., Das, A., Sobrido, A.B.J., Hing, K.A., Zayats, A.V., and Krause, S. (2022). Photoelectrochemical detection of calcium ions based on hematite nanorod sensors. ACS Appl. Nano Mat. *5*, 17087–17094.
6. Stett, A., Egert, U., Guenther, E., Hofmann, F., Meyer, T., Nisch, W., and Haemmerle, H. (2003). Biological application of microelectrode arrays in drug discovery and basic research. Anal. Bioanal. Chem. *377*, 486–495.
7. Sakmann, B., and Neher, E. (1984). Patch clamp techniques for studying ionic channels in excitable membranes. Annu. Rev. Physiol. *46*, 455–472.
8. Miccoli, B., Lopez, C.M., Goikoetxea, E., Putzeys, J., Sekeri, M., Krylychkina, O., Chang, S.W., Firrincieli, A., Andrei, A., Reumers, V., and Braeken, D. (2019). High-density electrical recording and impedance imaging with a multi-modal CMOS multi-electrode array chip. Front. Neurosci. *13*, 641.
9. Spira, M.E., and Hai, A. (2013). Multi-electrode array technologies for neuroscience and cardiology. Nat. Nanotechnol. *8*, 83–94.
10. Hafeman, D.G., Parce, J.W., and McConnell, H.M. (1988). Light-addressable potentiometric sensor for biochemical systems. Science *240*, 1182–1185.
11. Meng, Y., Chen, F., Wu, C., Krause, S., Wang, J., and Zhang, D.W. (2022). Light-addressable electrochemical sensors toward spatially resolved biosensing and imaging applications. ACS Sens. *7*, 1791–1807.
12. Owicki, J.C., Bousse, L.J., Hafeman, D.G., Kirk, G.L., Olson, J.D., Wada, H.G., and Parce, J.W. (1994). The light-addressable potentiometric sensor: Principles and biological applications. Annu. Rev. Biophys. *23*, 87–113.
13. Zhou, Y., Liu, E., Müller, H., and Cui, B. (2021). Optical electrophysiology: Toward the goal of label-free voltage imaging. J. Am. Chem. Soc. *143*, 10482–10499.
14. Hawe, A., Sutter, M., and Jiskoot, W. (2008). Extrinsic fluorescent dyes as tools for protein characterization. Pharm. Res. (N. Y.) *25*, 1487–1499.
15. O'Brien, J., Wilson, I., Orton, T., and Pognan, F. (2000). Investigation of the alamar blue (resazurin) fluorescent dye for the assessment of mammalian cell cytotoxicity. Eur. J. Biochem. *267*, 5421–5426.
16. Ulrich, G., Ziessel, R., and Harriman, A. (2008). The chemistry of fluorescent bodipy dyes: Versatility unsurpassed. Angew. Chem. Int. Ed. *47*, 1184–1201.
17. Brown, C.E., Aminoltejari, K., Erb, H., Winship, I.R., and Murphy, T.H. (2009). In vivo voltage-sensitive dye imaging in adult mice reveals that somatosensory maps lost to stroke are replaced over weeks by new structural and functional circuits with prolonged modes of activation within both the peri-infarct zone and distant sites. J. Neurosci. *29*, 1719–1734.
18. Chemla, S., and Chavane, F. (2010). Voltage-sensitive dye imaging: Technique review and models. J. Physiol. Paris *104*, 40–50.
19. Shoham, D., Glaser, D.E., Arieli, A., Kenet, T., Wijnbergen, C., Toledo, Y., Hildesheim, R., and Grinvald, A. (1999). Imaging cortical dynamics at high spatial and temporal resolution with novel blue voltage-sensitive dyes. Neuron *24*, 791–802.
20. Kuila, T., Bose, S., Khanra, P., Mishra, A.K., Kim, N.H., and Lee, J.H. (2011). Recent advances in graphene-based biosensors. Biosens. Bioelectron. *26*, 4637–4648.
21. Henriques, P.C., Pereira, A.T., Pires, A.L., Pereira, A.M., Magalhães, F.D., and Gonçalves, I.C. (2020). Graphene surfaces interaction with proteins, bacteria, mammalian cells, and blood constituents: The impact of graphene platelet oxidation and thickness. ACS Appl. Mater. Interfaces *12*, 21020–21035.
22. Balch, H.B., McGuire, A.F., Horng, J., Tsai, H.Z., Qi, K.K., Duh, Y.S., Forrester, P.R., Crommie, M.F., Cui, B., and Wang, F. (2021). Graphene electric field sensor enables single shot label-free imaging of bioelectric potentials. Nano Lett. *21*, 4944–4949.
23. Chu, C.H., Sarangadharan, I., Regmi, A., Chen, Y.W., Hsu, C.P., Chang, W.H., Lee, G.Y., Chyi, J.I., Chen, C.C., Shiesh, S.C., et al. (2017). Beyond the debye length in high ionic strength solution: direct protein detection with field-effect transistors (FETs) in human serum. Sci. Rep. *7*, 5256.
24. Lin, S.P., Pan, C.Y., Tseng, K.C., Lin, M.C., Chen, C.D., Tsai, C.C., Yu, S.H., Sun, Y.C., Lin, T.W., and Chen, Y.T. (2009). A reversible surface functionalized nanowire transistor to study protein–protein interactions. Nano Today *4*, 235–243.
25. Wrobel, G., Höller, M., Ingebrandt, S., Dieluweit, S., Sommerhage, F., Bochem, H.P., and Offenhäusser, A. (2008). Transmission electron microscopy study of the cell–sensor interface. J. R. Soc. Interface *5*, 213–222.
26. Jacques, R., Zhou, B., Marhuenda, E., Gorecki, J., Das, A., Iskratsch, T., and Krause, S. (2023). Photoelectrochemical imaging of single cardiomyocytes and monitoring of their action potentials through contact force manipulation of organoids. Biosens. Bioelectron. *223*, 115024.
27. Revel, J.P., and Karnovsky, M.J. (1967). Hexagonal array of subunits in intracellular junctions of the mouse heart and liver. J. Cell Biol. *33*, C7–C12.
28. Avila, J., Razado, I., Lorcy, S., Fleurier, R., Pichonat, E., Vignaud, D., Wallart, X., and Asensio, M.C. (2013). Exploring electronic structure of one-atom thick polycrystalline graphene films: A nano angle resolved photoemission study. Sci. Rep. *3*.
29. Jabbarzadeh, F., Heydari, M., and Habibzadeh-Sharif, A. (2019). A comparative analysis of the accuracy of kubo formulations for graphene plasmonics. Mater. Res. Express *6*, 086209.
30. Palik, E. (1997). List of contributors for volume i. In Handbook of Optical Constants of Solids, E.D. Palik, ed. (Academic Press). pp. xv–xvi.
31. Bockris, J.O., Gileadi, E., and Müller, K. (1966). Dielectric relaxation in the electric double layer. J. Chem. Phys. *44*, 1445–1456.
32. Zhang, X., Jing, Q., Ao, S., Schneider, G.F., Kireev, D., Zhang, Z., and Fu, W. (2020). Ultrasensitive field-effect biosensors enabled by the unique electronic properties of graphene. Small *16*, e1902820.
33. Fu, W., El Abbassi, M., Hasler, T., Jung, M., Steinacher, M., Calame, M., Schönenberger, C., Puebla-Hellmann, G., Hellmüller, S., Ihn, T., and Wallraff, A. (2014). Electrolyte gate dependent high-frequency measurement of graphene field-effect transistor for sensing applications. Appl. Phys. Lett. *104*, 013102.
34. Chen, E., Goldbeck, R.A., and Kliger, D.S. (1997). Nanosecond time resolved spectroscopy of biomolecular processes. Annu. Rev. Biophys. *26*, 327–355.
35. Castro Neto, A.H., Guinea, F., Peres, N.M.R., Novoselov, K.S., and Geim, A.K. (2009). The electronic properties of graphene. Rev. Mod. Phys. *81*, 109–162.
36. Li, Z.Q., Henriksen, E.A., Jiang, Z., Hao, Z., Martin, M.C., Kim, P., Stormer, H.L., and Basov, D.N. (2008). Dirac charge dynamics in graphene by infrared spectroscopy. Nat. Phys. *4*, 532–535.
37. Mak, K.F., Sfeir, M.Y., Wu, Y., Lui, C.H., Misewich, J.A., and Heinz, T.F. (2008). Measurement of the optical conductivity of graphene. Phys. Rev. Lett. *101*, 196405.
38. Yan, H., Xia, F., Zhu, W., Freitag, M., Dimitrakopoulos, C., Bol, A.A., Tulevski, G., and Avouris, P. (2011). Infrared spectroscopy of wafer-scale graphene. ACS Nano *5*, 9854–9860.

STAR★METHODS

KEY RESOURCES TABLE

REAGENT or RESOURCE	SOURCE	IDENTIFIER
Software and algorithms		
Computational Codes	This Publication	https://doi.org/10.5281/zenodo.8422649
MATLAB 2023	MathWorks	www.mathworks.com

RESOURCE AVAILABILITY

Lead contact

Further information and requests for resources and reagents should be directed to and will be fulfilled by the lead contact, Jon Gorecki (J.Gorecki@imperial.ac.uk).

Materials availability

The work presented in this paper did not generate any new materials.

Data and code availability

(1) This paper does not report original data.
(2) All code (written in MATLAB format) used in this manuscript to produce figures are publicly available to be accessed freely from Zenodo Data Repository at https://doi.org/10.5281/zenodo.8422649.
(3) Any additional information required to reanalyze the data reported in this paper is available from the lead contact upon request.

EXPERIMENTAL MODEL AND STUDY PARTICIPANT DETAILS

This work did not include any experimental model or study participants.

METHOD DETAILS

Calculation of graphene conductivity

The interactions of graphene are modeled by the Kubo equations which describe the complex frequency dependent conductivity as a function of Fermi energy and carrier mobility. When an incident photon is absorbed by graphene there are two possible types of band transition which can happen; inter-band transitions, and intra-band transitions. Photons at visible and NIR wavelengths will generally have sufficient energy to excite an inter-band transition where an electron is excited from valence to conduction band, while at longer wavelengths the photons will cause intra-band transitions where an electron moves within its initial energy band. The equations for the inter and intra band transitions of shown in Equations 4 and 5 respectively, where the charge carrier scattering time τ is 0.1 ps, which corresponds to a carrier mobility value of $10,000\ cm^2/Vs$.

$$\sigma_{inter} = \frac{e^2}{\pi\hbar}\left[1 + \frac{i}{\pi} ln\left(\frac{\hbar(\omega+i\tau^{-1})-2E_f}{\hbar(\omega+i\tau^{-1})+2E_f}\right)\right] \quad \text{(Equation 4)}$$

$$\sigma_{intra} = \frac{ie^2}{\pi\hbar^2}\frac{E_f}{\omega+i\tau^{-1}} \quad \text{(Equation 5)}$$

At visible wavelengths the electronic (and therefore optical) properties are dominated by the inter-band transitions which are essentially constant and unaffected by the graphene Fermi energy, while at long wavelengths (FIR and THz) the electronic properties are dominated by intra-band transitions and are strongly dependent on Fermi energy. For practical imaging devices it is preferable to operate in the visible/NIR region where wavelengths are smaller (and therefore spatial resolution is increased) and there are a range of mature technologies for the emission, control, and detection of visible wavelength light. Due to the nature of the inter-band transitions graphene is unsuitable for electrostatic sensing at visible wavelengths, however there is a crossing point at which the inter and intra-band transitions change their dominance, which results in a sharp step-like feature in the electrical conductivity.

In Figure S1 the real and imaginary components of the graphene conductivity are plotted for a range of wavelengths and Fermi energies. To provide a general intuitive relation between the complex conductivity and the optical properties, the real conductivity relates to optical attenuation while the imaginary conductivity relates to phase delay of an optical pulse. Figure S1A plots the real conductivity of graphene at three different Fermi energies for a range of wavelengths from the visible to THz region on a logarithmic x axis. At short wavelengths the

conductivity is dominated the by inter-band transitions and is invariant to changes in Fermi energy. Around 1 μm there is a sharp step-like feature where the inter-band transitions suddenly become forbidden due to the Pauli blocking effect (it is forbidden to excite an electron into a higher filled energy state), and moves to shorter wavelengths as the Fermi energy increases. At long wavelengths the intra-band transitions dominate and show an exponential-like curve. Figure S1B plots the imaginary conductivity which again shows two distinct regions where the inter and intra-band transitions independently dominate. Figures S1C and S1D shows the real and imaginary conductivity in the vicinity of the Pauli blocking feature. This spectral crossover region between inter-band and intra-band transitions is well understood from theory[35] and has been experimentally verified by a number of groups[36–38] which has been observed to occur in the region of 1–3 μm, where the location of the feature is dependent on the graphene Fermi energy.[37]

Figures S1E and S1F plot the real and imaginary conductivity as a surface plot against wavelength and Fermi energy to gain further understanding of the behavior around the Pauli blocking feature. It can be seen for the real conductivity that this feature essentially creates a binary function of high and low conductivity, while for the imaginary component there is a smoother variation of conductivity.

Calculating device reflectivity

Equation 6 describes the Fresnel transmission coefficient for light passing from medium *a* with complex refractive index $\tilde{n}_a$ into medium *b*. Equation 7 describes the Fresnel reflection coefficient as light reflecting within medium a, bounded by medium b. Equation 8 describes the attenuation as a beam passes through a medium of thickness d, where ω is the angular frequency of the light, and *c* is the speed of light. Equation 9 is known as the Tinkham reflection coefficient which describes light reflecting off of a graphene monolayer within a medium with complex refractive index, bounded by air on the other side of the graphene. z_0 is the vacuum impedance, and σ is the complex frequency dependent conductivity of the graphene.

$$T_{ab} = \frac{2\tilde{n}_a}{\tilde{n}_a+\tilde{n}_b} \quad \text{(Equation 6)}$$

$$R_{ab} = \frac{\tilde{n}_a - \tilde{n}_b}{\tilde{n}_a+\tilde{n}_b} \quad \text{(Equation 7)}$$

$$P_d = exp(-i\tilde{n}\omega d/c) \quad \text{(Equation 8)}$$

$$R_g = \frac{1-\tilde{n}-z_0\sigma}{\tilde{n}+1+z_0\sigma} \quad \text{(Equation 9)}$$

To find the total reflected pulse it is necessary to add together the first, second, third … (and so on to infinity) reflected pulses together; this infinite sum can conveniently be calculated to an exact value with a Taylor series, where the total reflected pulse *X* is given in Equation 10, where silicon is denoted as medium a, and silicon dioxide is denoted as medium b.

$$X = \frac{T_{ab}\,T_{ba}}{R_{ba}}\left[\frac{1}{1-P_{2d}\,R_g\,R_{ba}}-1\right]+R_{ab} \quad \text{(Equation 10)}$$

The resultant light pulse described by *X* will give the complex electric field, however at visible wavelengths it is not possible to measure the electric field of light directly in the time domain detectors only can measure the time averaged intensity. This value can be found by multiplying the complex field by its complex conjugate as shown in Equation 11 where X^* is the complex conjugate of *X*.

$$X_{TimeAvg.} = \Re[XX^*] \quad \text{(Equation 11)}$$

Determining device spatial resolution

To investigate the issue of spatial resolution of the graphene device a finite-element simulation is performed in Comsol Multiphysics. The simulation models the case of two charged objects (cubes of side length 10 μm) which are sitting at a distance of 2 nm above a grounded plane. This scenario is analogous to two charged cells in the vicinity of a graphene sheet. The model is solved for various distances of separation between the two charged objects, and the induced surface charge on the graphene sheet is plotted. It can be seen for 32 μm separation the charges induced in the graphene make two distinct peaks, however as the objects are brought into close proximity the peaks begin to overlap. It is not possible to make a direct analogy here to the Rayleigh definition for optical resolution which is defined as the maximum of one peak overlapping with the first minimum of the second peak, as in our case the features do not have minima. Instead we highlight the object separation of 4 μm as the point in which the peak surface charge of the first peak falls to half its maximum value before mixing into the second peak. This model does not include the effects of ionic screening, which could only serve to improve the resolution as they will limit long-range effects of electrostatic fields.

QUANTIFICATION AND STATISTICAL ANALYSIS

This article does not include statistical analysis.